36． Young and embedded clusters in Cygnus-X: evidence for building up the initial mass function?
MNRAS 458, 3027–3046 (2016)
Francisco F. S. Maia, Estelle Moraux and Isabelle Joncour

We provide a new view on the Cygnus-X north complex by accessing for the first time the low mass content of young stellar populations in the region. Canada–France–Hawaii Telescope/Wide-Field Infrared Camera was used to perform a deep near-infrared survey of this complex, sampling stellar masses down to ~0.1 $M_\odot$. Several analysis tools, including a extinction treatment developed in this work, were employed to identify and uniformly characterize a dozen unstudied young star clusters in the area. Investigation of their mass distributions in low-mass domain revealed a relatively uniform log-normal initial mass function (IMF) with a characteristic mass of 0.32 ± 0.08 $M_\odot$ and mass dispersion of 0.40 ± 0.06. In the high-mass regime, their derived slopes showed that while the youngest clusters (age < 4 Myr) presented slightly shallower values with respect to the Salpeter's, our older clusters (4 Myr < age < 18 Myr) showed IMF compliant values and a slightly denser stellar population. Although possibly evidencing a deviation from an 'universal' IMF, these results also supports a scenario where these gas-dominated young clusters gradually 'build up' their IMF by accreting low-mass stars formed in their vicinity during their first ~3 Myr, before the gas expulsion phase, emerging at the age of ~4 Myr with a fully fledged IMF. Finally, the derived distances to these clusters confirmed the existence of at least three different star-forming regions throughout Cygnus-X north complex, at distances of 500–900 pc, 1.4–1.7 and 3.0 kpc, and revealed evidence of a possible interaction between some of these stellar populations and the Cygnus OB2 association.

Cygnus-X north 領域

Cyg OB2
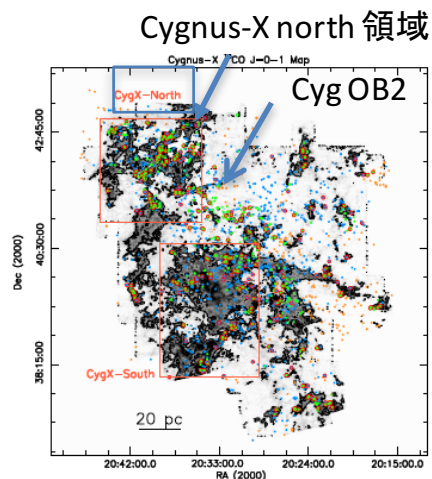
Cygnus-X north 領域、低質量星0.1M◦までclusterごとのIMF を比較。
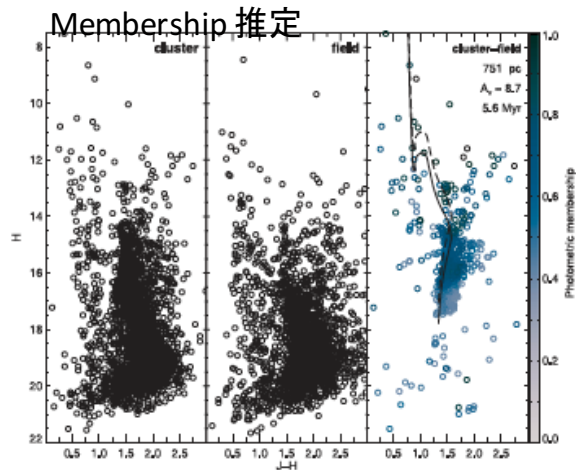Wide-Field Infrared Camera (WIRCam) @ CFHT
JHKs3色測光

Membership 推定
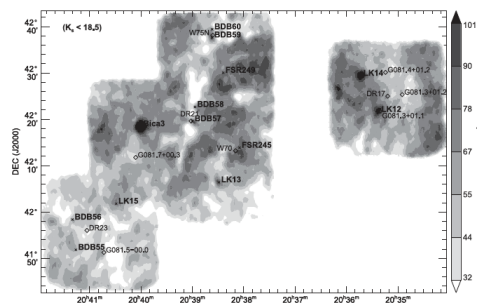
Figure 8. CMD comparing the samples in LK12 region (left-hand panel), in its nearby field (middle panel) and the field-subtracted sample (right-hand panel). The colour bar shows the assigned photometric probabilities. Isochrones representing the single star (solid line) and equal mass unresolved binaries (dashed line) populations are shown, along with the most probable age, distance and extinction inferred.

$$P_{phot} = \frac{\rho_{clu} - \rho_{fld}}{\rho_{clu}}, \qquad (4)$$

where ρ_{clu} and ρ_{fld} represent the local stellar density in the cluster and field samples, respectively, taken at the same position in the multicolour space. The method can also benefit from a 1D posi-
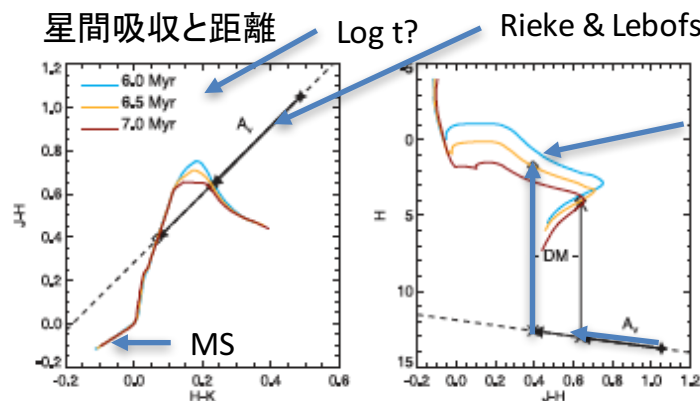
$M>0.7M_\odot$

$M<0.7M_\odot$

Figure 10. Results of the extinction determination showing (a) the adopted isochrone (solid line) and the intrinsic colours of LK12 stars, dereddend using the expected extinction value for the population. Most stars (plus signs) were assigned to their lower mass intercept in the isochrone while a few bluer ones (diamonds) where assigned to the higher mass intercept. The derived extinction values were interpolated into a local extinction map (b), with the colour bar indicating the extinction levels, and used to construct the global extinction (c) and distance modulus distributions (d) for LK12 stars from which their expected values (dashed lines) were derived.

星間吸収と距離   Log t?   Rieke & Lebofskyのextinction law

PARSEC 星の進化 0.1M$_\odot$~300M$_\odot$

Avは2値：選択
年齢とdistant modulus 分散が小さくなるように？

Avは2値

MS

Figure 9. Colour–colour (left) and colour–magnitude (right) diagrams comparing solar metallicity isochrones of log t 6.0, 6.5 and 7.0. It shows how the reddening vector (dashed lines) can be used to derive both the extinction and distance modulus for a particular star, given its possible isochrone intercepts (diamonds).
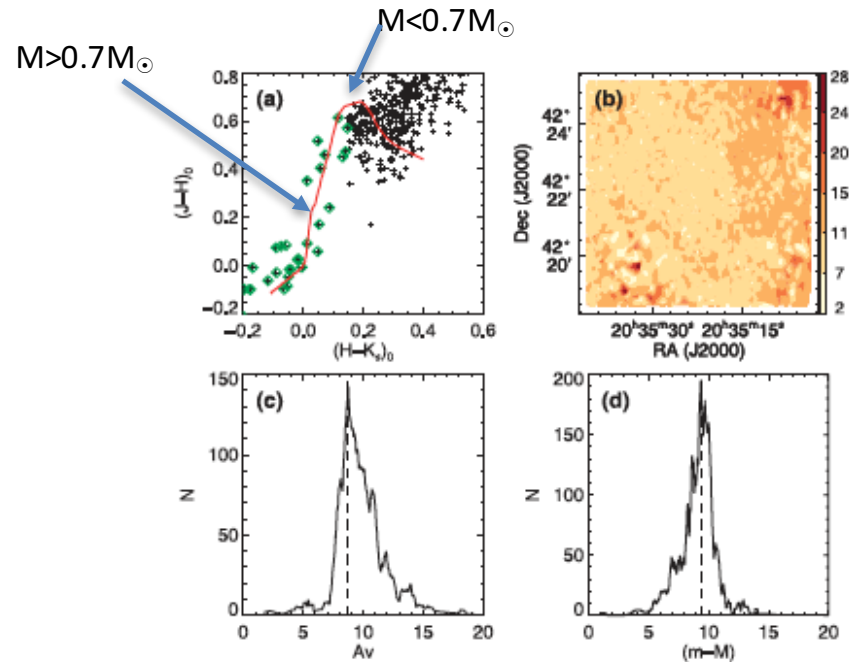
$$\xi(m) = \frac{dN}{dm} = \frac{A}{m} \exp\left[-\frac{(\log m - \log m_c)^2}{2\sigma_m^2}\right], \quad m \leq 1\,M_\odot$$
$$= A\,k\,m^{-\alpha}, \quad m \geq 1\,M_\odot, \quad (12)$$

ID	RA (h:m:s)	Dec. (°:′:″)	$\bar{\rho}$ (pc⁻²)	r_c (pc)	r_t (pc)	Age (Myr)	A_v	D (kpc)	Mass ($M_\odot$)	m_c ($M_\odot$)	σ_m (log $M_\odot$)	α
LK12	20:35:22	42:21:54	174 ± 18	0.29 ± 0.02	0.92 ± 0.07	4–9	8.73 ± 0.07	0.65–0.83	318–441	0.34 ± 0.04	0.34 ± 0.02	2.44 ± 0.10
LK14	20:35:42	42:29:31	274 ± 40	0.23 ± 0.03	0.84 ± 0.10	9–18	8.49 ± 0.04	0.92–1.12	433–621	0.38 ± 0.13	0.30 ± 0.04	2.08 ± 0.10
FSR249	20:38:29	42:29:15	100 ± 39	0.44 ± 0.19	0.93 ± 0.33	7–13	7.00 ± 0.12	1.45–1.75	312–458	0.38 ± 0.19	0.39 ± 0.08	1.83 ± 0.11
LK13	20:38:29	42:06:22	922 ± 101	0.08 ± 0.01	0.25 ± 0.01	4–6	7.19 ± 0.06	0.45–0.55	38–46	0.20 ± 0.06	0.35 ± 0.03	1.98 ± 0.34
BDB59	20:38:37	42:37:29	77 ± 17	0.18 ± 0.03	0.72 ± 0.11	1–3	12.95 ± 0.03	1.15–1.38	224–274	0.22 ± 0.12	0.50 ± 0.09	1.41 ± 0.32
BDB58	20:38:54	42:22:44	46 ± 6	0.40 ± 0.10	1.30 ± 0.10	1–3	13.47 ± 0.06	2.74–3.34	610–772	0.30 ± 0.10	0.37 ± 0.07	1.53 ± 0.29
BDB57	20:39:02	42:19:37	117 ± 63	0.04 ± 0.01	0.40 ± 0.15	1–3	24.40 ± 0.06	0.60–0.78	163–218	0.18 ± 0.10	0.46 ± 0.07	1.36 ± 0.12
Bica3	20:40:01	42:18:17	12 ± 1	1.34 ± 0.11	3.85 ± 0.25	~500	15.10 ± 0.10	4.49–5.10	~3000	–	–	1.33 ± 0.14
LK15	20:40:30	42:03:13	70 ± 22	0.44 ± 0.16	1.02 ± 0.28	1–3	11.18 ± 0.18	1.65–2.13	367–475	0.55 ± 0.26	0.33 ± 0.11	1.67 ± 0.10
BDB56	20:41:19	41:58:09	97 ± 22	0.15 ± 0.01	0.58 ± 0.06	2–5	9.80 ± 0.13	1.39–1.61	140–186	0.41 ± 0.18	0.40 ± 0.08	1.79 ± 0.11

若い星団　α~1.xx
4Myr以上の星団　α~2.xx Salpeterと一致

解釈
初期<3Myrに形成済みの低質量星がガスの効果
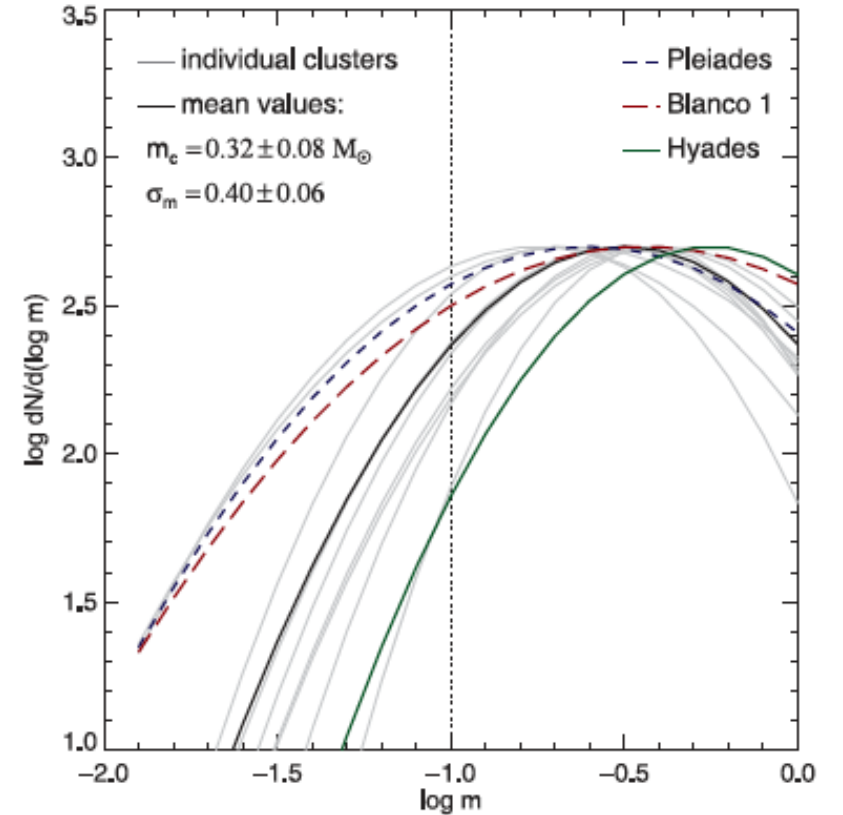で星団に落下しSalpeter的べきを作る。
ガスが4Myr程度で晴れ、その後は進化しなくなる。

Figure 19. Comparison of the individual (thin lines) and mean (thick line) log-normal mass functions derived in this work with the reference values (dashed lines) for the Pleiades, Blanco1 and Hyades clusters. The vertical dotted line represents the minimum mass sampled in our IMFs (0.1 $M_\odot$).

On the Formation of Super-Earths with Implications for the Solar System
Rebecca G. Martin and Mario Livio

We first consider how the level of turbulence in a protoplanetary disk affects the formation locations for the observed close-in super-Earths in exosolar systems. We find that a protoplanetary disk that <u>includes a dead zone (a region of low turbulence) has substantially more material in the inner parts of the disk</u>, possibly allowing for in situ formation. For the dead zone to last the entire lifetime of the disk <u>requires the active layer surface density to be sufficiently small, <100 g/cm^2</u>. Migration through a dead zone may be very slow and thus super-Earth formation followed by migration towards the star through the dead zone is less likely. <u>For fully turbulent disks</u>, there is not enough material for in situ formation. However, in this case, <u>super-Earths can form farther out in the disk and migrate inwards</u> on a reasonable timescale. We suggest that both of these formation mechanisms operate in different planetary systems. This can help <u>to explain the observed large range in densities of super-Earths because the formation location determines the composition</u>. Furthermore, we speculate that super-Earths could have formed in the inner parts of our solar system and cleared the material in the region inside of Mercury's orbit. The super-Earths could migrate through the gas disk and fall into the Sun if the disk was sufficiently cool during the final gas disk accretion process. While it is definitely possible to meet all of these requirements, we don't expect them to occur in all systems, which may explain why the solar system is somewhat special in its lack of super-Earths.
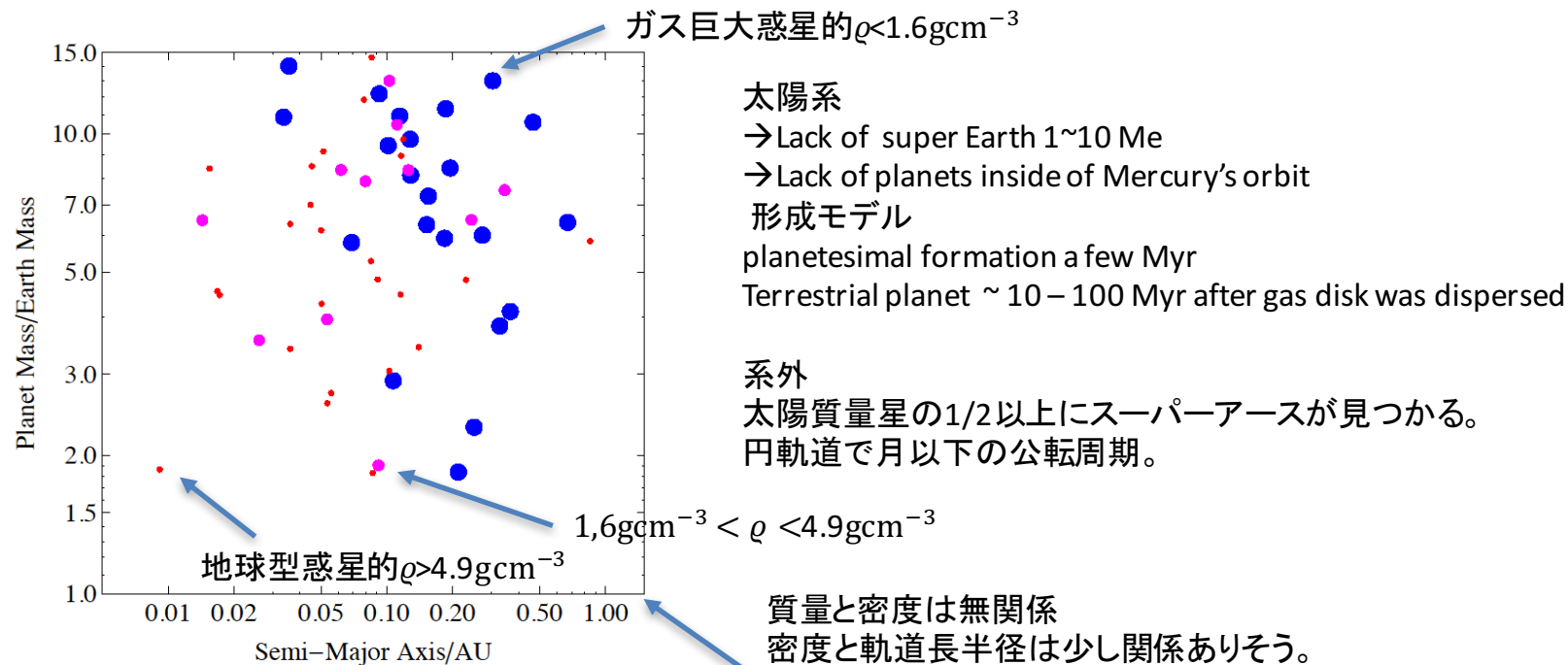
ガス巨大惑星的 $\varrho < 1.6 \mathrm{gcm}^{-3}$

太陽系
→Lack of super Earth 1~10 Me
→Lack of planets inside of Mercury's orbit
形成モデル
planetesimal formation a few Myr
Terrestrial planet $\sim 10 - 100$ Myr after gas disk was dispersed

系外
太陽質量星の1/2以上にスーパーアースが見つかる。
円軌道で月以下の公転周期。

$1,6 \mathrm{gcm}^{-3} < \varrho < 4.9 \mathrm{gcm}^{-3}$

地球型惑星的 $\varrho > 4.9 \mathrm{gcm}^{-3}$

質量と密度は無関係
密度と軌道長半径は少し関係ありそう。

Figure 1. Planet mass and semi–major axis of the observed exoplanets with a mass in the range $1 \mathrm{M}_{\oplus} < M_{\mathrm{p}} < 15 \mathrm{M}_{\oplus}$ that have a density measurement. The large (blue) points denote planets with a low density $\rho \leq 1.6 \mathrm{g\,cm}^{-3}$, the medium–size (magenta) points denote those with a density in the range $1.6 \mathrm{g\,cm}^{-3} < \rho < 3.9 \mathrm{g\,cm}^{-3}$ and the small (red) points denote those with a high density, $\rho > 3.9 \mathrm{g\,cm}^{-3}$. For reference, in our solar system the terrestrial planets have average densities $\rho > 3.9 \mathrm{g\,cm}^{-3}$ and the giant planets have average densities $\rho < 1.6 \mathrm{g\,cm}^{-3}$. Data are from exoplanets.org.

ガス円盤が残っているうちに巨大惑星的スーパーアースが形成されたのか？
形成場所、
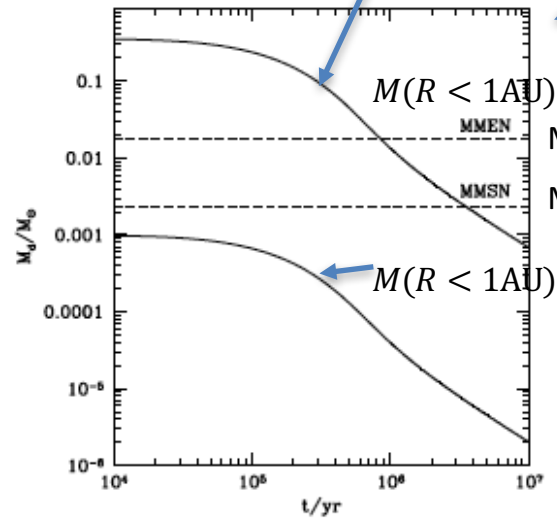（1）その場形成
（2）雪線外部で形成され、内側に運ばれた。

全乱流ディスク

$M(R < 40\text{AU})$

$\alpha = 0.01$ディスク
乱流ディスクではその場形成する固体成分は不十分、

モデル2

$M(R < 1\text{AU})$

Minimum-mass extrasolar nebula

Minimum-mass solar nebula

$M(R < 1\text{AU})$

$$\tau_{\text{type I}} \approx 6.7 \times 10^5 \left(\frac{M_{\text{p}}}{5\,\text{M}_\oplus}\right)^{-1} \left(\frac{M}{1\,\text{M}_\odot}\right)^{-\frac{3}{2}} \left(\frac{a}{1\,\text{AU}}\right)^{-\frac{1}{2}}$$
$$\times \left(\frac{\Sigma}{100\,\text{gcm}^{-2}}\right)^{-1} \left(\frac{H/R}{0.05}\right)^2 \text{yr}$$

Figure 2. Disk mass up to a radius of $R = 1$ AU as a function of time (lower line) and total disk mass up to a radius of 40 AU (upper line). The initial disk surface density is a steady state fully turbulent disk with an infall accretion rate of 1×10^{-5} M$_\odot$ yr^{-1}. The infall accretion rate decreases exponentially in time according to equation (10). The dashed lines show the mass in $R < 1$ AU for the MMSN (lower) and the MMEN (upper).
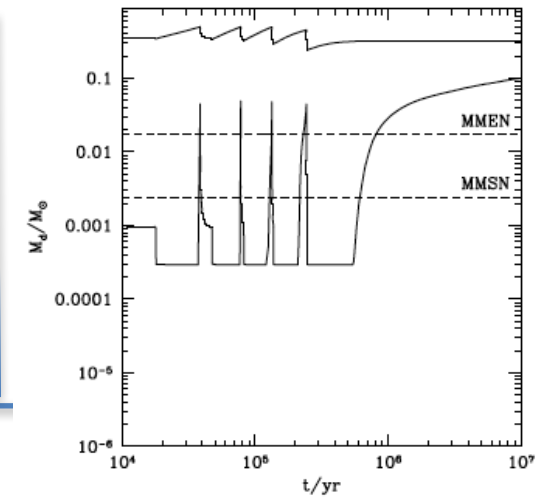
Figure 6. Same as Fig. 2 except the disk has a dead zone defined by model 2 with $Re_{\text{M,crit}} = 5 \times 10^4$ (bottom right).

Dead-Zoneあり乱流ディスク
モデル1
$\Sigma < \Sigma_{crit}$あるいは$T > T_{crit}$の時MRIがON。
Off領域がDead-zone
CR: $\Sigma_{crit} \sim 200\text{g}cm^{-3}$ Xray: さらに少。

モデル2
レイノルズ数$R = \frac{\sqrt{\alpha}c_S H}{\eta}$ $\eta = 234\sqrt{T_c}/x_e\,\text{cm}^2\text{s}^{-1}$を求め
ならDead-zone

モデル1
CR: $\Sigma_{crit} \sim 200\text{g}cm^{-3}$
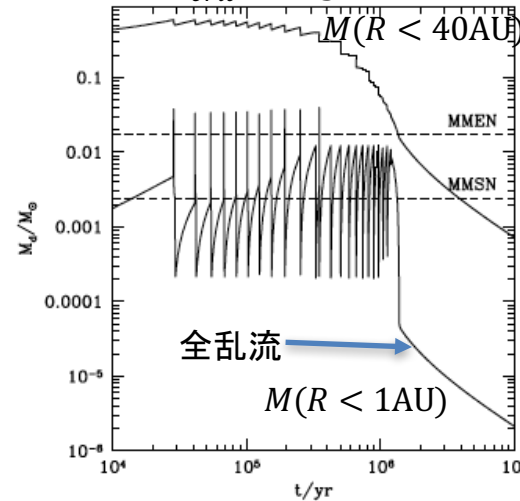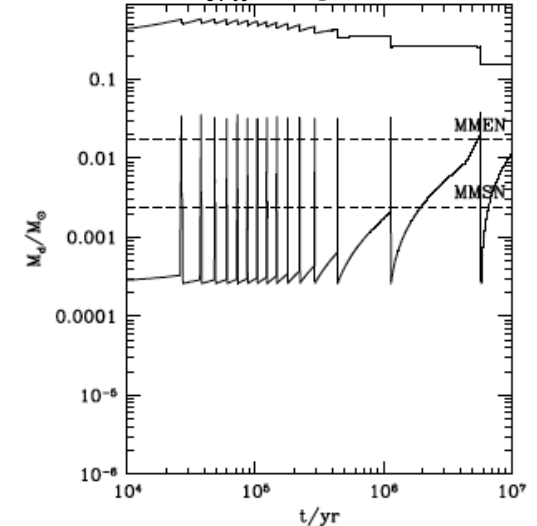
$M(R < 40\text{AU})$

全乱流

$M(R < 1\text{AU})$

Figure 3. Same as Fig. 2 except the disk has a dead zone defined by mod with $\Sigma_{\text{crit}} = 200$ g cm^{-2} and $T_{\text{crit}} = 800$ K.

モデル1
UV: $\Sigma_{crit} \sim 20\text{g}cm^{-3}$

Figure 4. Same as Fig. 2 except the disk has a dead zone defined by model 1 with $\Sigma_{\text{crit}} = 20$ g cm^{-2} and $T_{\text{crit}} = 800$ K.

Photo-reverberation Mapping of a Protoplanetary Accretion Disk around a T Tauri Star
Huan Y. A. Meng et al

Theoretical models and spectroscopic observations of newborn stars suggest that protoplantary disks have an inner "wall" at a distance set by the disk interaction with the star. Around T Tauri stars, the size of this disk hole is expected to be on a 0.1-AU scale that is unresolved by current adaptive optics imaging, though some model-dependent constraints have been obtained by near-infrared interferometry. Here we report the first measurement of the inner disk wall around a solar-mass young stellar object, YLW 16B in the {¥rho} Ophiuchi star-forming region, by detecting the light travel time of the variable radiation from the stellar surface to the disk. Consistent time lags were detected on two nights, when the time series in H (1.6 {¥mu}m) and K (2.2 {¥mu}m) bands were synchronized while the 4.5 {¥mu}m emission lagged by 74.5 +/- 3.2 seconds. Considering the nearly edge-on geometry of the disk, the inner rim should be 0.084 AU from the protostar on average, with an error of order 0.01 AU. This size is likely larger than the range of magnetospheric truncations, and consistent with an optically and geometrically thick disk front at the dust sublimation radius at ~1500 K. The widths of the cross-correlation functions between the data in different wavebands place possible new constraints on the geometry of the disk.

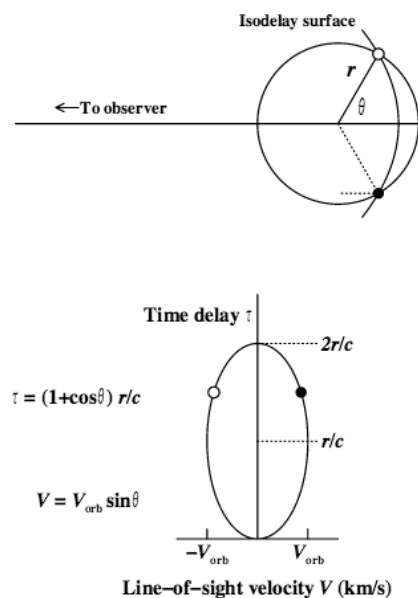B.M. Peterson and K. Horne: *Reverberation Mapping of AGNs*　　3

FIGURE 1. *Upper diagram:* In this simple, illustrative model, the line-emitting clouds are taken to be on a circular orbit of radius r around the central black hole. The observer is to the left. In response to an instantaneous continuum outburst, the clouds seen by the distant observer at a time delay τ after detection of the continuum outburst will be those that lie along an "isodelay surface," for which the time delay relative to the continuum signal will be $\tau = (1 + \cos\theta)r/c$, the length of the dotted path shown. *Lower diagram:* The circular orbit is mapped into the line-of-sight velocity/time-delay plane.

Reverberation mapping
AGNの質量推定

$$M_{AGN} = R_{BLR}V^2/G$$

R_BLRは、AGNからの連続光の変光からBLR 雲起源の輝線の変光までの時間差によって、推定する。

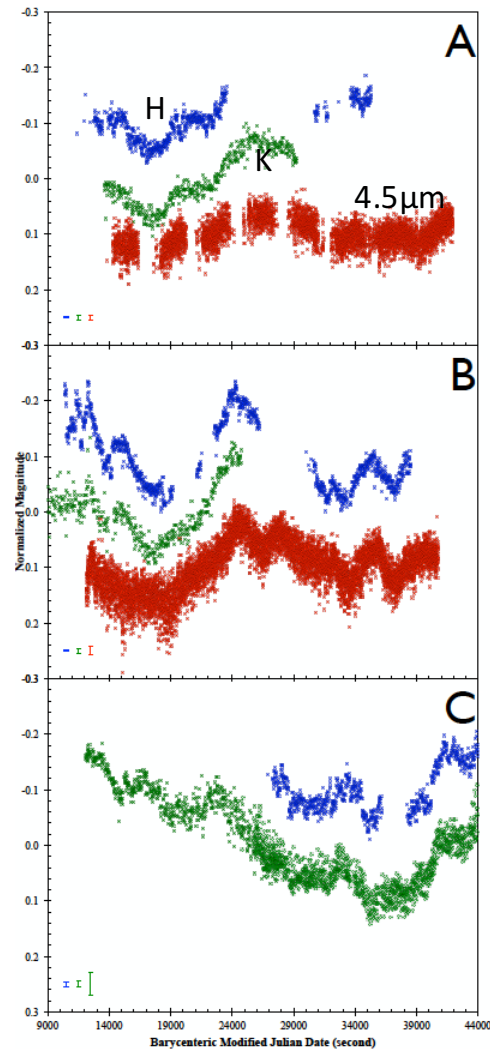ρOph cloud 内YLW16B TTauri型星
ディスク中央穴の大きさは0.1pc程度、近赤外の干渉計でも測定できない。

同時観測
Spitzer IRAC ➔ 4.5μm
Mayall 4mφ / FLAMINGOS
SOAR 4mφ / Spartan IR Camera ➔ Hバンド
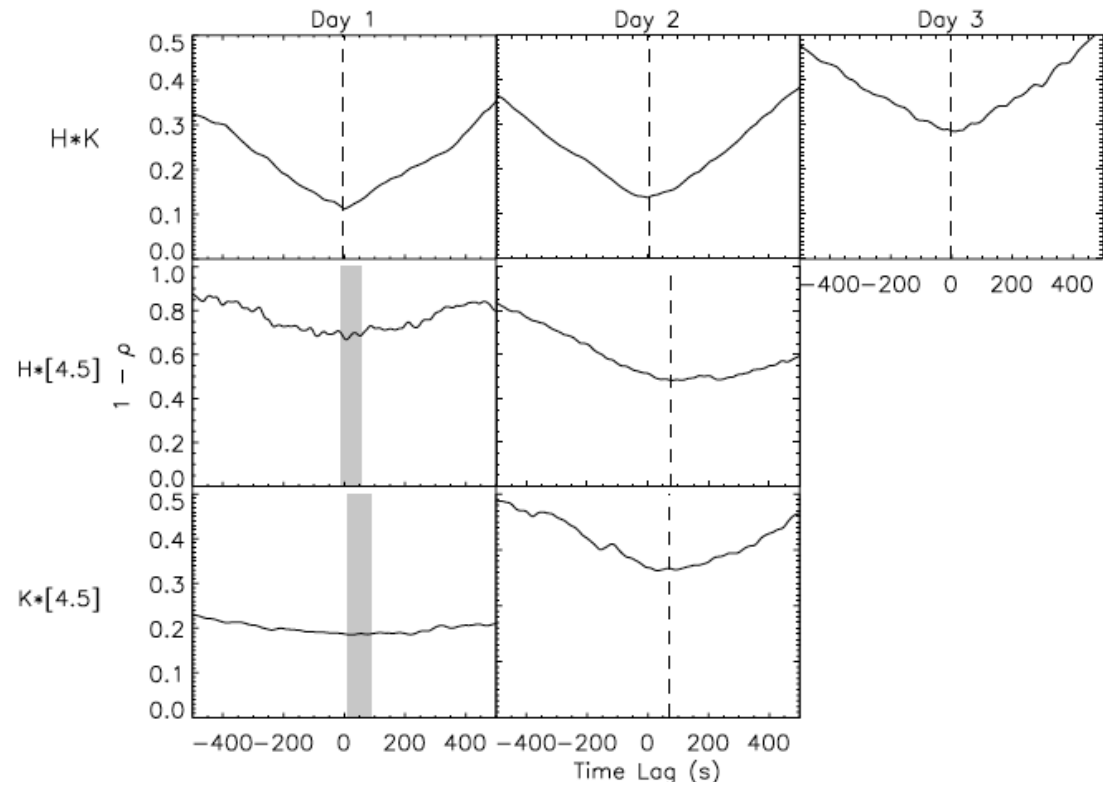1.3mφ、1.5mφ ➔ K バンド

A

H

K

4.5μm

B

C

Figure 4. Cross-correlation functions of YLW 16B between the H, K, and 4.5 μm time series. The data are shown in time lag (in seconds) vs $1 - \rho$, where ρ is the corresponding cross correlation function. the plots are aligned vertically for the day of observations, and horizontally for the pair of compared wavebands. The measurements of time lags with errors smaller than 5 seconds are labeled with vertical dashed lines; the 1σ error ranges of those with larger errors are shaded. The $H \star K$ cross correlations are consistent with a zero time lag within the errors, while the 4.5 μm data lag behind both H and K by a consistent amount of time, 74.5 ± 3.2 seconds.

$$\frac{\int_0^\pi R_{in} \sin^2 \theta d\theta}{\int_0^\pi \sin \theta d\theta} = \frac{\pi}{4} R_{in} \qquad (13)$$

$$R_{in}(1 + \frac{\pi}{4})$$

$$\int_0^\pi R_{in}(1 + sin\theta)sin\theta d\theta$$

θ

R_{in}

$(((74.5 \text{ second} * c) / AU) * \pi) / 4 = 0.11725772$

$R_{in} = 0.084 \pm 0.004 AU$

➔ Disk 昇華（1500K）半径ではないか

Dynamical ejections of massive stars from young star clusters under diverse initial conditions
Seungkyung Oh and Pavel Kroupa

We study the effects of initial conditions of star clusters and their massive star population on dynamical ejections of stars from star clusters up to an age of 3 Myr, particularly focusing on massive systems, using a large set of direct N-body calculations for moderately massive star clusters (Mecl=$10^{3.5}$ Msun). We vary the initial conditions of the calculations such as the initial half-mass radius of the clusters, initial binary populations for massive stars and initial mass segregation. We find that the initial density is the most influential parameter for the ejection fraction of the massive systems. The clusters with an initial half-mass radius of 0.1 (0.3) pc can eject up to 50% (30)% of their O-star systems on average. Most of the models show that the average ejection fraction decreases with decreasing stellar mass. For clusters efficient at ejecting O stars, the mass function of the ejected stars is top-heavy compared to the given initial mass function (IMF), while the mass function of stars remaining in the cluster becomes slightly steeper (top-light) than the IMF. The top-light mass functions of stars in 3 Myr old clusters in our N-body models are in good agreement with the mean mass function of young intermediate mass clusters in M31 as found by Weisz et al.. We show that the multiplicity fraction of the ejected massive stars can be as high as 60%, that massive high-order multiple systems can be dynamically ejected, and that high-order multiples become common especially in the cluster. Furthermore, binary populations of the ejected massive systems are discussed. When a large survey of the kinematics of the field massive stars becomes available, e.g through Gaia, our results may be used to constrain the birth configuration of massive stars in star clusters.
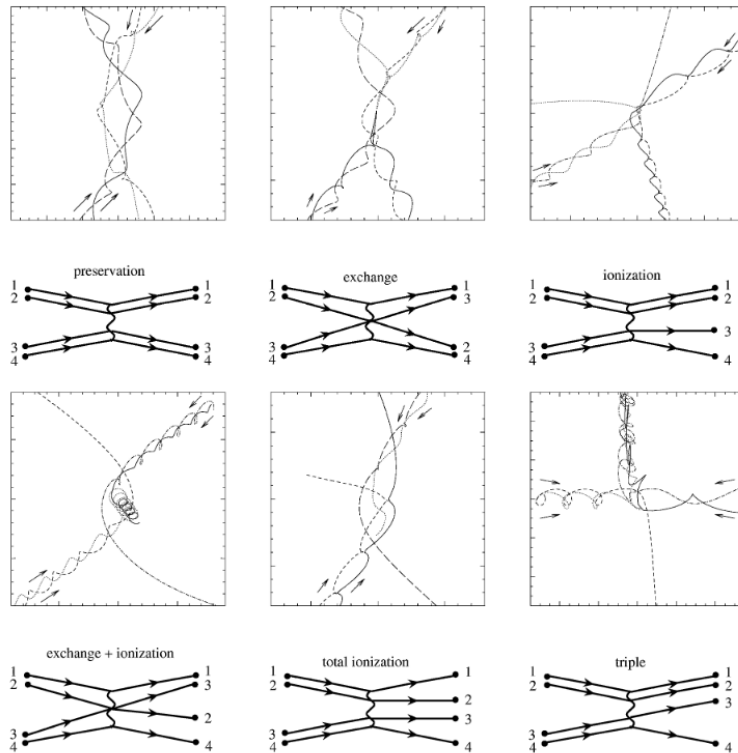
Figure 2. Examples of different outcomes in binary–binary scattering events and the corresponding Feynman diagrams. In the diagrams, the paths of two stars are placed close together when they are bound, and the wavy lines represent gravitational perturbations.
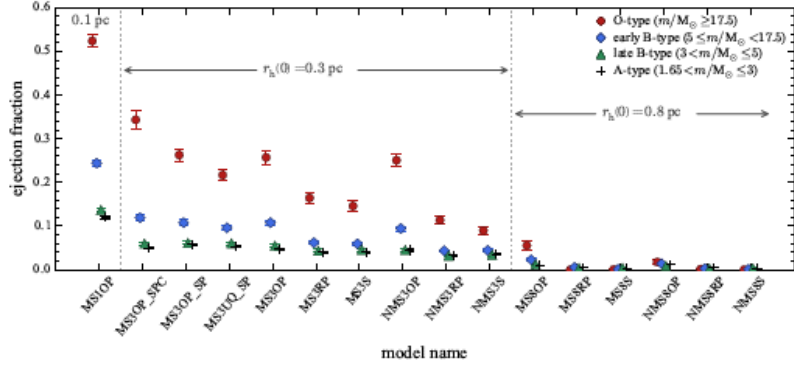
Fig. 1. Averaged ejection fractions (Eq. 4), $\langle f_{ejST} \rangle$, of systems for four different primary-mass groups at 3 Myr. Model names are indicated on the x-axis (see Table 1). The error bars are the standard deviation of the mean.
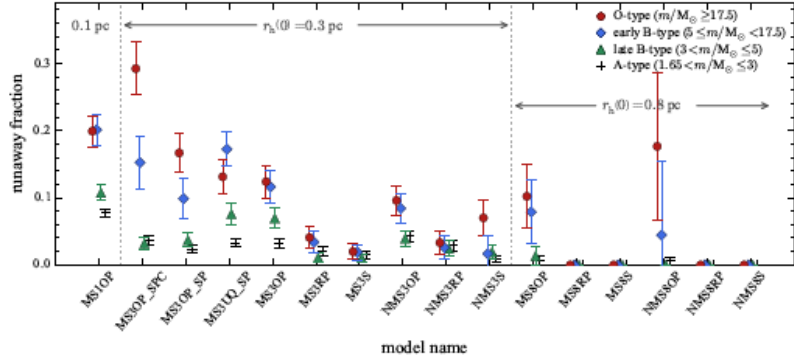

Fig. 2. Runaway fraction among the ejected systems, the number of runaways divided by the number of ejected stars (Eq. 5). The fraction is derived from all runs for each model. The error bars indicate Poisson uncertainties.
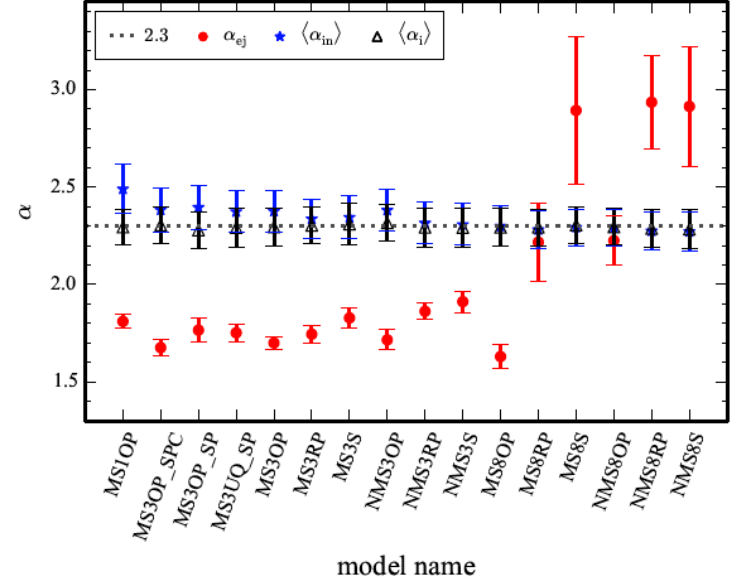

Fig. 8. Mass function slopes for all (individual) stars with mass $\geq 2\,M_\odot$. Red filled circles are the present-day mass functions for the ejected stars (α_{ej}). Blue stars are the averaged present-day mass function slopes of the stars remaining in the clusters at 3 Myr ($\langle\alpha_{in}\rangle$), while black open triangles are those at 0 Myr (i.e. IMF, $\langle\alpha_i\rangle$). The canonical value of the upper IMF, $\alpha_2 = 2.3$ (Eq. 1), is marked with a dotted grey line.

Mass segregation in star clusters is not energy equipartition
Richard J. Parker, Simon P. Goodwin, Nicholas J. Wright, Michael R. Meyer and Sascha P. Quanz

Mass segregation in star clusters is often thought to indicate the onset of energy equipartition, where the most massive stars impart kinetic energy to the lower-mass stars and brown dwarfs/free floating planets. The predicted net result of this is that the centrally concentrated massive stars should have significantly lower velocities than fast-moving low-mass objects on the periphery of the cluster. We search for energy equipartition in initially spatially and kinematically substructured N-body simulations of star clusters with N = 1500 stars, evolved for 100 Myr. In clusters that show significant mass segregation we find no differences in the proper motions or radial velocities as a function of mass. The kinetic energies of all stars decrease as the clusters relax, but the kinetic energies of the most massive stars do not decrease faster than those of lower-mass stars. These results suggest that dynamical mass segregation - which is observed in many star clusters - is not a signature of energy equipartition from two-body relaxation.

Mass segregation: 大質量星が中心に、小質量星が周辺に分布。
$\sigma \propto m^{-0.5}$ ← $m\sigma^2 \sim$ 一定　完全エネルギー等分配
　　〃　　　的　　　　　　　部分エネルギー等分配

エネルギー等分配にかかる時間（Spitzer 1969）
t_relax=(N/8 ln N) t_cross
t_cross〜0.1Myr　t_relax〜100Myr　N=1000

これが本当に起こっているかを調べた。
初期条件
fractal dimension D=1.6
ヴィリアル比αvir=K/|W|=0.3
0.01 M8 < M <50 M8
N=1500 stars

図2　もとの構造を再帰的に分割することで得られるシェルピンスキーの三角形

$$D = \lim_{\epsilon \to 0} \frac{\log N(\epsilon)}{\log \left(\frac{1}{\epsilon}\right)} = \lim_{k \to \infty} \frac{\log 3^k}{\log 2^k} = \frac{\log 3}{\log 2} \approx 1.585$$

εを1/2にすると、構造3倍増えるとき

Mass segregation ratio
  $\Lambda\_MSR = <l\_ave> / <l\_sub>$
  $<l\_sub>$最大質量N_MST個の星の間の平均距離、
  $<l\_ave>$任意のN_MST個の星の間の平均距離

$\Lambda\_MSR=1$ 質量分離なし
$\Lambda\_MSR>>1$ 強い質量分離

$$E=\frac{1}{2}mv^2$$

質量分離

(a) Evolution of Λ_{MSR}

質量分離なし

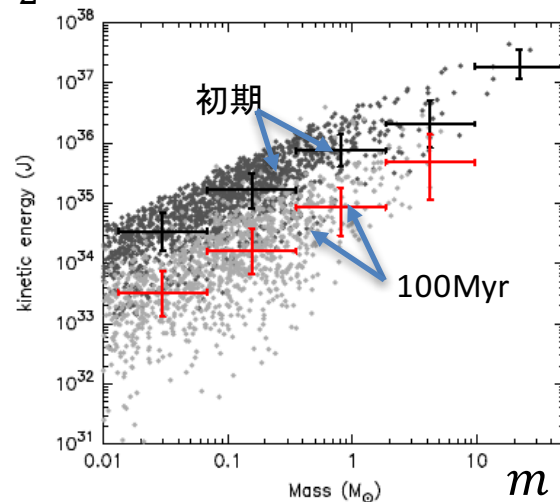時間進化

最重量10星程度
が強く質量分離

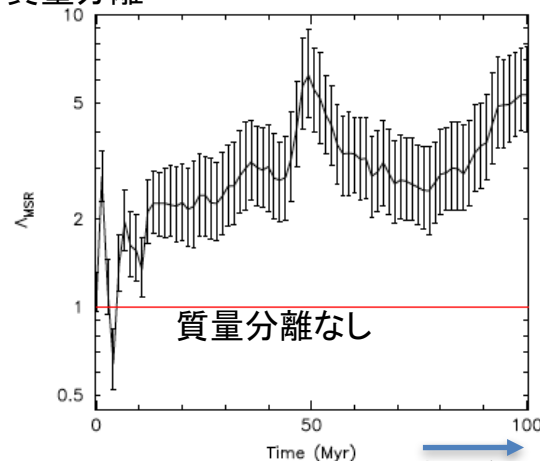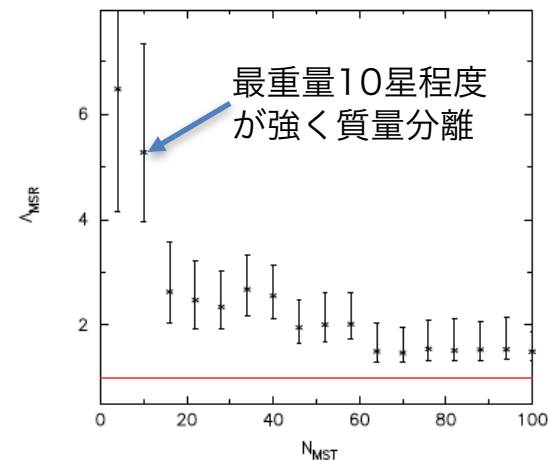(b) Λ_{MSR} ; 100 Myr

初期

100Myr

m

Figure 4. Kinetic energy as a function of stellar mass for the initial conditions (dark grey points) and at 100 Myr (light grey points). The median kinetic energies for equally spaced mass intervals are shown by the error bars, where the horizontal error bars indicate the mass range, and the vertical error bars are the interquartile range of kinetic energies. The black error bars are for the initial conditions; the red error bars are the values at 100 Myr.

結論
質量分離は見えるが、エネルギー等分配には見えない